Naval Research Laboratory

Washington, DC 20375-5320

NRL/MR/6791--20-10,122

Simulation Case Study of Gamma-ray Production from Laser-Solid Interactions at Ultrarelativistic Intensity

Abdurrahman H. Younis

Department of Physics, University of Rochester
Rochester, NY

Asher W. Davidson

NRC Postdoctoral
Washington, DC

Bahman Hafizi

Daniel F. Gordon

Beam Physics Branch
Plasma Physics Division

August 11, 2020

REPORT DOCUMENTATION PAGE

Form Approved
OMB No. 0704-0188

1. REPORT DATE *(DD-MM-YYYY)*	**2. REPORT TYPE**	**3. DATES COVERED** *(From - To)*
11-08-2020	NRL Memorandum Report	June 2019 – June 2020

4. TITLE AND SUBTITLE

Simulation Case Study of Gamma-ray Production from Laser-Solid Interactions at Ultrarelativistic Intensity

5a. CONTRACT NUMBER

5b. GRANT NUMBER

5c. PROGRAM ELEMENT NUMBER

6. AUTHOR(S)

Abdurrahman H. Younis*, Asher W. Davidson**, Bahman Hafizi, and Daniel F. Gordon

5d. PROJECT NUMBER

5e. TASK NUMBER

5f. WORK UNIT NUMBER
4781

7. PERFORMING ORGANIZATION NAME(S) AND ADDRESS(ES)

Naval Research Laboratory
4555 Overlook Avenue, SW
Washington, DC 20375-5320

8. PERFORMING ORGANIZATION REPORT NUMBER

NRL/MR/6791--20-10,122

9. SPONSORING / MONITORING AGENCY NAME(S) AND ADDRESS(ES)

Office of High Energy Physics
SC-25.1/Germantown Building
U.S. Department of Energy
1000 Independence Avenue, SW
Washington, DC 20585-1290

10. SPONSOR / MONITOR'S ACRONYM(S)

DOE

11. SPONSOR / MONITOR'S REPORT NUMBER(S)

12. DISTRIBUTION / AVAILABILITY STATEMENT

DISTRIBUTION STATEMENT A: Approved for public release; distribution is unlimited.

13. SUPPLEMENTARY NOTES

*Department of Physics, University of Rochester, 500 Wilson Blvd, Rochester, NY 14627
** NRC Postdoctoral, 500 Fifth Street, N.W., Washington, DC 20001

14. ABSTRACT

The emission of multi-MeV (gamma ray) photons from the interaction of a high-powered laser with a tailored plasma target is studied using particle-in-cell simulations. The plasma and pulse characteristics that produce a bright γ-flare are described, and results from two state-of-the-art codes are presented. The maximum laser-to-gamma energy conversion efficiency obtained is 30%, which is consistent with published results. The mechanism responsible for such high-energy photons is also discussed.

15. SUBJECT TERMS

Gamma rays X-rays
Laser Simulation

16. SECURITY CLASSIFICATION OF:			**17. LIMITATION OF ABSTRACT**	**18. NUMBER OF PAGES**	**19a. NAME OF RESPONSIBLE PERSON**
a. REPORT	**b. ABSTRACT**	**c. THIS PAGE**			Daniel Gordon
Unclassified Unlimited	Unclassified Unlimited	Unclassified Unlimited	Unclassified Unlimited	29	**19b. TELEPHONE NUMBER** *(include area code)* (202) 767-5036

Standard Form 298 (Rev. 8-98)
Prescribed by ANSI Std. Z39.18

This page intentionally left blank.

CONTENTS

EXECUTIVE SUMMARY E-1

1. INTRODUCTION 1

2. THEORY 2
   2.1 Photon Emission 2
   2.2 Pair Creation 4

3. METHOD 5
   3.1 Particle-in-Cell Algorithm 5
   3.2 Quantum Electrodynamics Subroutines 6
   3.3 Particle Merging 7
   3.4 Covariant Propagation 8
   3.5 Simulation Setup 8

4. RESULTS 9
   4.1 Gamma-ray Energy Dependence Parametric Scan 10
   4.2 High-efficiency Case: OSIRIS vs. EPOCH 13

5. CONCLUSION 18

ACKNOWLEDGMENTS 19

REFERENCES 19

APPENDIX A—On the Electron Quantum Parameter 21
   A.1 Plane Electromagnetic Wave 21
   A.2 Static Magnetic Field 22

FIGURES

1 Feynman diagram for nonlinear Compton scattering 3

2 Nonlinear Thomson scattering cross section 3

3 Synchrotron emissivity function 7

4 General simulation setup 9

5 Longitudinal intensity envelope and plasma profiles 9

6 Total γ energy vs. pre-plasma length 10

7 Electron charge density after laser-plasma interaction 10

8 Simulation setup: High-efficiency case 13

9 OSIRIS: Energy fraction vs. time 14

10 EPOCH: Energy fraction vs. time 14

11 Particle energy spectrum 14

12 Field amplitude and radiation-reaction parameter vs. time 14

13 Photon energy and radiated power vs. time 15

14 Spectrum of radiated emission by electrons 15

15 Electron momentum distribution 16

16 Electron quantum parameter in-simulation 16

17 Average γ energy and density 17

18 Angular distribution of emitted γ-rays 17

A1 Electromagnetic wave incident on an electron beam 23

A2 Electron quantum parameter vs. relative angle 23

TABLES

1 Energy conversion efficiency vs. pre-plasma length 10

2 Energy conversion efficiency vs. target thickness 11

3 Energy conversion efficiency vs. pulse duration 11

4 Laser intensity parameters..... 12

5 Energy conversion efficiency vs. laser intensity 12

6 Energy conversion efficiency vs. laser polarization 12

This page intentionally left blank.

EXECUTIVE SUMMARY

The emission of multi-MeV (gamma ray) photons from the interaction of a high-powered laser with a tailored plasma target is studied using particle-in-cell simulations. The plasma and pulse characteristics that produce a bright γ-flare are described, and results from two state-of-the-art codes are presented. The maximum laser-to-gamma energy conversion efficiency obtained is 30%, which is consistent with published results. The mechanism responsible for such high-energy photons is also discussed.

This page intentionally left blank.

SIMULATION CASE STUDY OF GAMMA-RAY PRODUCTION FROM LASER-SOLID INTERACTIONS AT ULTRARELATIVISTIC INTENSITY

1. INTRODUCTION

In the coming years, the development of high-powered laser technology will reach the multi-petawatt scale with peak intensities approaching 10^{24} W/cm^2. At laboratories such as the Extreme Light Infrastructure (ELI) facilities in Europe, and the University of Rochester's Laboratory for Laser Energetics (LLE) in the United States, major developmental projects to reach the multi-petawatt regime are under way. In particular, Rochester's LLE plans to upgrade their existing OMEGA EP laser system by the year 2025. OMEGA EP will be used to pump an ultra-intense optical parametric chirped-pulse amplification (OPCPA) system called EP OPAL, which is expected to produce 15 fs pulses with 3 kJ of energy, corresponding to a peak power of 200 PW and focused intensities of $\sim 10^{24}$ W/cm^2 [1, 2] . Such ultra high-intensity lasers will enable the investigation of novel areas of physics, such as vacuum nonlinear optics [3] and quantum electrodynamics (QED) plasma physics [4]. Additional technological applications include table-top particle accelerators, advanced isotope sources, and ultra-fast imaging systems. It is truly an exciting era for research in laser-matter interaction and high-energy-density physics.

In this report, we focus on laser-plasma interaction and its ability to produce energetic photons. The processes responsible for high-energy photon emission are bremsstrahlung due to electron-ion scattering [5], magneto-bremsstrahlung induced by a high plasma current [6, 7], and, in the intensity regime where radiation reaction effects become dominant ($I \simeq 10^{23}$ W/cm^2), nonlinear Compton scattering from direct interaction between electrons and the strong electromagnetic field [8]. The typical energy of these outgoing photons is on the hundred-MeV scale, which lies in the γ range. Further interaction of the emitted γ-rays with background laser photons, or the electrostatic field of a high-Z nucleus, can result in electron-positron pair creation via the Breit-Wheeler or Bethe-Heitler process, respectively [9–11]. If the efficiency of this process can be increased, a QED-plasma of electrons and positrons will form. Thus, efficient conversion of the incident pulse energy into γ-rays is desirable in order to produce this unique state of matter in a laboratory setting.

Below, we present our results from two-dimensional particle-in-cell (PIC) simulations in order to understand the process of γ-ray emission via nonlinear Compton scattering. This work constitutes a preliminary investigation for upcoming three-dimensional simulations. As will be discussed, there are multiple plasma and pulse characteristics which must be taken into consideration when optimizing the γ-ray conversion efficiency. A systematic study of these key parameters is presented along with results which illustrate the dependence of the total γ energy. Since empirical data is not available yet, we employ two different PIC codes, OSIRIS [12] and EPOCH [13], to study this phenomenon. Although the two codes employ different Monte-Carlo emission algorithms, they are in agreement with regards to the conversion efficiency magnitude.

Manuscript approved Month 00, 2020.

The rest of this report is organized as follows. In Section 2, we review the theory underlying nonlinear Compton scattering and other processes of interest. In Section 3, we outline the basics of particle-in-cell codes and discuss the manner in which OSIRIS and EPOCH handle QED calculations. In Section 4, simulation results are presented, and in Section 5 we summarize our work and outline future directions.

2. THEORY

2.1 Photon Emission

For an electron irradiated by an intense electromagnetic wave, the mechanism responsible for γ-ray emission is nonlinear Compton scattering. This process occurs when the relativistically-invariant parameter

$$a_0 = e\sqrt{-A_\mu A^\mu}/mc^2 \tag{1}$$

is significantly greater than unity, where e and m are the electron charge magnitude and mass, c is the speed of light, and A^μ is the 4-vector potential of the laser field. An electron at rest encountering a pulse with $a_0 \gg 1$ will be ponderomotively accelerated to relativistic energy $\mathscr{E} = \gamma mc^2$ in a single laser cycle, where $\gamma = \sqrt{1+(\vec{p}/mc)^2}$ is the Lorentz factor associated with electron momentum $\vec{p}$. Moreover, a_0 gives the energy absorbed by the electron $\Delta\mathscr{E} = eE_0\lambda_c$ in one Compton wavelength ($\lambda_c = h/mc \simeq 2.43\times10^{-12}$ m) in units of the laser photon energy $\hbar\omega$, where E_0 is the field amplitude of frequency ω. The probability of emission also depends on the quantum parameter

$$\eta = \frac{e\hbar}{m^3c^4}|F_{\mu\nu}p^\nu| \equiv \frac{E_{\rm rf}}{E_s} \tag{2}$$

in which $p^\nu = (\mathscr{E}/c, \vec{p})$ is the electron 4-momentum, $F_{\mu\nu} = \partial_\mu A_\nu - \partial_\nu A_\mu$ is the electromagnetic field tensor, $E_{\rm rf} \sim \gamma E \sim a_0 E$ is the field in the electron rest frame, and $E_s = m^2c^3/\hbar e \simeq 1.32\times10^{18}$ V/m is the Schwinger critical field.

Nonlinear Compton scattering occurs when the electron absorbs $n\omega$ laser photons and emits a single high-energy photon ω_γ, i.e.,

$$e^- + n\omega \rightarrow e^- + \omega_\gamma.$$

This process is illustrated in Fig. 1. The electron enters the field with 4-momentum p^μ and interacts with laser photons all of the same wave vector k^μ. It emits a single photon k'^μ and departs with 4-momentum p'^μ. In cases where $\hbar\omega_\gamma/\gamma mc^2 \ll 1$, radiation reaction effects are negligible and the behavior is described in the classical regime of nonlinear Thomson scattering. In the limit $\hbar\omega_\gamma/\gamma mc^2 \sim 1$, the electron recoil may *not* be neglected, and the process is referred to as nonlinear Compton scattering. In Fig. 2, the dependence of the nonlinear Thomson scattering cross section $\sigma_{\rm NTS}$ on the normalized field amplitude a_0 is shown. The parameter $\varepsilon_{\rm rad} = 4\pi r_e/3\lambda$ gives the field amplitude above which radiation damping *cannot* be neglected: $a_0 = \varepsilon_{\rm rad}^{-1/3}$ where $r_e = e^2/mc^2$ is the classical electron radius, and we use a wavelength of $\lambda = 1$ μm. For the range of field amplitudes $a_0 \lesssim \varepsilon_{\rm rad}^{-1/3}$, the scattering cross section increases as $\sigma_{\rm NTS} \simeq \sigma_t(1+a_0^2)$ where $\sigma_t = 8\pi r_e^2/3 \simeq 6.65\times10^{-25}$ cm^2 is the Thomson scattering cross section. It reaches a maximum of $\sigma_{\rm NTS} \simeq 0.53\,\sigma_t\,\varepsilon_{\rm rad}^{-2/3}$ at $a_0 = 1.1\,\varepsilon_{\rm rad}^{-1/3} \simeq 450$. For $a_0 \gg \varepsilon_{\rm rad}^{-1/3}$, the cross section decreases according to

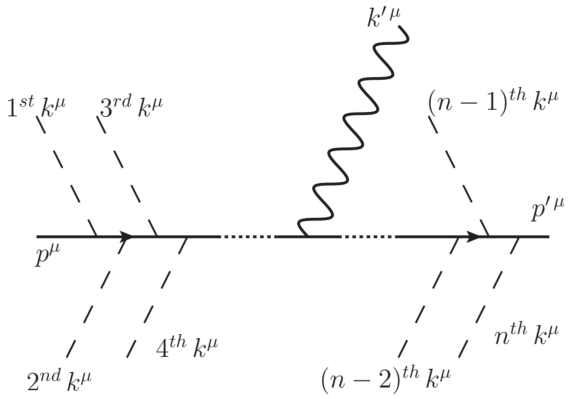

Fig. 1—Feynman diagram for multiphoton Compton scattering. Reprinted with permission from Ref. [14].

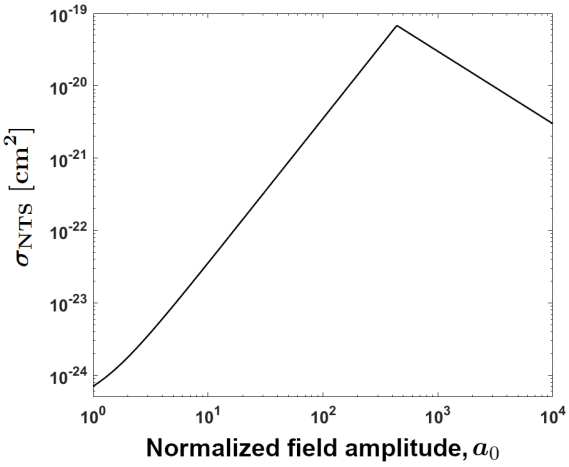

Fig. 2—Nonlinear Thomson scattering cross section versus field amplitude.

$\sigma_{\mathrm{NTS}} \simeq \sigma_t / a_0 \varepsilon_{\mathrm{rad}}$, which is due to the fact that the maximum power re-emitted by the electron cannot exceed $P = eE_0 c$. Consequently, the scattering cross section is maximized when the radiation reaction friction force parameter $a_0 \varepsilon_{\mathrm{rad}}^{1/3}$ satisfies: $1 \lesssim a_0 \varepsilon_{\mathrm{rad}}^{1/3} \lesssim 1.1$. For more details, see Ref. [15] and sources contained therein. In what follows, we will ignore the difference in terminology with Thomson scattering, in which quantum effects are negligible, and refer to the process generally as nonlinear Compton scattering.

As the laser field in this process is extremely intense, a perturbative treatment is not appropriate. Moreover, an exact treatment would require one to sum over all n photons in Fig. 1, making the calculation intractable from a theoretical sense. Instead, calculations are performed in the Furry picture of quantum dynamics [16] in which the laser field is accounted for intrinsically by dressing the electron wavefunction. The states are obtained as solutions to the Dirac equation with a plane wave vector potential term:[1]

$$\left\{\gamma_\mu \left[i\partial^\mu - eA^\mu(\phi)\right] - m\right\}\psi_{\boldsymbol{p}\sigma} = 0 \tag{3}$$

where γ_μ are the Dirac matrices, A^μ describes the background plane wave, which depends only on the phase $\phi = k_\mu x^\mu$, and $\psi_{\boldsymbol{p}\sigma}$ is the electron spinor wavefunction. Solutions to Eq. (3) were obtained in 1935, and are the familiar Volkov states [17]:

$$\psi_{\boldsymbol{p}\sigma}(x) = \frac{1}{\sqrt{2\mathscr{E}V}}\left[1 + \frac{e\not{k}\not{A}}{2(kp)}\right] u_{\boldsymbol{p}\sigma} e^{iS} \tag{4}$$

where $u_{\boldsymbol{p}\sigma}$ is the free-electron spinor and S is the classical action,

$$S = -(px) - \int_{-\infty}^{\phi} d\phi' \left\{ e\frac{[pA(\phi')]}{(kp)} - \frac{e^2 A^2(\phi')}{2(kp)} \right\} \tag{5}$$

[1] The following set of equations employ natural units, $\hbar = c = 1$.

and we have employed Feynman slash notation $\not{k} \equiv \gamma_\mu k^\mu$ with $(px) \equiv p_\mu x^\mu$. The generic scattering matrix for arbitrary γ-ray and lepton states,

$$S_{fi} = -ie \int \bar{\psi}_f(x) \not{A}(x) \psi_i(x) d^4x \tag{6}$$

where the initial and final bispinors $\psi_i(x)$ and $\bar{\psi}_f(x)$ represent electrons, and A^μ is the 4-vector potential of γ-rays generated by the nonlinear Compton process, can be expressed as:

$$S_{fi} = -ie \int \bar{\psi}_{\boldsymbol{p}'\sigma'} \gamma_\mu \psi_{\boldsymbol{p}\sigma} \sqrt{4\pi} \frac{\varepsilon'^\mu}{\sqrt{2\omega V}} e^{ik'_\mu x^\mu} d^4x \tag{7}$$

which can be used to calculate the emission cross section of a photon with polarization ε'^μ by an electron with four-momenta p^μ and p'^μ before and after scattering, respectively [14].

Another method by which laser-plasma interaction can produce gamma ray photons is bremsstrahlung radiation, which requires a dense medium inside of which the energetic electrons can scatter [5]. In a recent experiment performed at the Texas Petawatt Laser (TPW) facility, a 150 fs laser pulse with a peak intensity of $I \simeq 10^{21}$ W/cm^2 was fired at solid Au targets several millimeters in thickness, producing a laser-to-gamma energy conversion efficiency of 4% [18]. However, for next-generation multi-petawatt laser systems, kinetic simulations indicate that a conversion efficiency in excess of 10% can be obtained. Two explanations, supported by numerical results, for the enhanced γ-ray production rate exist. The first theory is based on nonlinear Compton scattering and the interaction of an ultrashort 10 PW pulse with a tailored hydrogen target [19]. The second theory is based on the laser-induced plasma magnetic field causing photon emission via magnetic bremsstrahlung radiation [6, 7]. In the latter case, the target is a cylindrical channel with an interior region that serves as an optical waveguide, delivering a well-directed photon beam with a 5° opening angle.

In this work, we investigate the γ-ray emission process in the radiation-reaction-dominated regime involving nonlinear Compton scattering. We perform two-dimensional kinetic simulations using the configuration of Ref. [19] and compare the results of two PIC codes, obtaining broad agreement in the energy conversion efficiency magnitude. Calculations are performed to demonstrate that the induced plasma current is too weak for magnetic bremsstrahlung to efficiently convert electron energy into γ-ray photons. However, it must be noted that this result holds only for our particular target geometry, plasma profile characteristics, and laser pulse properties.

2.2 Pair Creation

Breit-Wheeler pair production is a physical process in which an electron-positron pair is created from the interaction of two photons,

$$\gamma\gamma' \rightarrow e^+ e^-.$$

Due to the high energy required of the colliding photons, and the low interaction probability, the pure Breit-Wheeler process has not been observed experimentally. However, the interaction between high-energy

γ-rays and laser photons from upcoming multi-petawatt facilities will bring us closer to generating electron-positron beams via the *multiphoton* Breit-Wheeler process. The multiphoton, or nonlinear, Breit-Wheeler process is described by the interaction of a single γ-ray with $n\omega$ coherent laser photons,

$$\gamma + n\omega \rightarrow e^+ e^-.$$

It has been demonstrated experimentally, to low order, by the head-on collision of a 46.6 GeV electron beam with terawatt pulses from an Nd:glass laser operating at a peak intensity of 10^{18} W/cm^2 [20]. Another method which makes use of the multiphoton Breit-Wheeler mechanism involves generating an ultra-relativistic electron beam via wakefield acceleration, then employing the bremsstrahlung γ-rays emitted from the electron's interaction with a high-Z target to create electron-positron pairs [21]. We briefly describe these pair-creation methods to highlight an important application of high-energy γ-rays. In what follows, we will concentrate exclusively on the nonlinear Compton scattering process. For a treatment of the theory of pair creation, refer to [10, 11, 22].

3. METHOD

In order to study how the interaction of a laser pulse with a plasma target can produce γ-rays, we performed two-dimensional particle-in-cell simulations. PIC methods have a long history in the study of laser-plasma interactions. See Refs. [23, 24] for an extensive review of the core algorithm.

3.1 Particle-in-Cell Algorithm

To summarize, PIC codes operate by tracking the motion of macro-particles, each of which represents many physical particles through a weight quantity. The physical significance of the macro-particle is that it characterizes real particles whose dynamical behavior in the plasma is approximately the same. Consequently, the computational burden of tracking particles is reduced, and the task of numerically modeling laser-plasma interactions becomes feasible. At each time-step of the simulation, the PIC algorithm proceeds as follows. First, the relativistic Lorentz equation of motion is integrated to update the position and velocity of each macro-particle. Then, the charge and current densities are interpolated onto the grid mesh. The fields are computed on the mesh points, after which they are interpolated back to the macro-particle positions to be used in the next cycle. The field mesh-interpolation stage is the most time-consuming part of the PIC algorithm, so its accuracy and efficiency are critical, and a great deal of effort is spent on optimizing the various schemes. Generally, particle-pushing schemes can be categorized as either implicit or explicit. The former calculates particle velocities from already updated fields, while the latter depends only on previous time-step information. Implicit solvers offer the advantage of being computationally stable at the expense of longer computation time between steps, while explicit solvers are fast but unstable.

There are many more complexities when it comes to the design of a PIC code, such as the distribution of particles in a cell, the algorithm to use for the pusher, how to handle inter-particle collisions, the inclusion of separate routines to model physical effects, and so on. In this paper, we will discuss the particular cases of (1) modeling nonlinear QED, (2) an algorithm to merge and reduce the number of macro-particles, and (3) the implementation of a covariant propagation scheme.

3.2 Quantum Electrodynamics Subroutines

The two PIC codes employed in this work, OSIRIS and EPOCH, have QED modules that are operationally different. To be more precise, the stochastic nature of photon emission necessitates a Monte-Carlo algorithm, and it is this portion of the calculation where the two codes differ. The PIC method encompasses all possible field configurations by taking advantage of the fact that in the local constant field approximation, the cross sections of all processes merge into a single expression: that of an electron in a constant, crossed field, provided the electron is relativistic.

The photon emission rate by an electron moving in a field of strength $E = bE_s$ is given by

$$\frac{d^2N}{d\chi\, dt} = \sqrt{3}\frac{mc^2}{\hbar}\alpha b\frac{F(\eta,\chi)}{\chi} \tag{8}$$

where $\alpha = e^2/\hbar c$ is the fine-structure constant, and

$$F(\eta,\chi) = \frac{4\chi^2}{\eta^2}yK_{2/3}(y) + \left(1-\frac{2\chi}{\eta}\right)y\int_y^\infty dt\, K_{5/3}(t) \tag{9}$$

is the synchrotron function which depends on the quantum parameters

$$\eta = \frac{e\hbar}{m^3c^4}|F_{\mu\nu}p^\nu| \tag{10}$$

$$\chi = \frac{e\hbar^2}{2m^3c^4}|F_{\mu\nu}k^\nu| \tag{11}$$

where $y = 4\chi/[3\eta(\eta-2\chi)]$, and K_n are the modified Bessel functions of the second kind. Equations (10) and (11) determine the importance of nonlinear QED effects for electrons and photons, respectively. Specifically, the η parameter can be used to calculate the probability of photon emission by an electron (or positron), and likewise for the χ parameter and the probability of pair-creation by a photon. The quantum parameter of the emitted particle, whether it is a photon (χ) or an electron-positron pair (η), also factors into the probability for the associated process to occur. A plot of the synchrotron emissivity function $F(\eta,\chi)$ is provided in Fig. 3. For more details, see Refs. [25, 26] and sources contained therein for alternative formulations of the synchrotron function.

3.2.1 OSIRIS

OSIRIS is a fully relativistic, massively parallel particle-in-cell code developed and maintained by the OSIRIS consortium, which consists of the Extreme Plasma Physics Group at Instituto Superior Tècnico in Portugal, and the Plasma Simulation Group at the University of California, Los Angeles. The OSIRIS-QED algorithm uses the following distribution to determine the quantum parameter of radiated photons:

$$\frac{d^2P}{dt\, d\chi_\gamma} = \frac{\alpha mc^2}{\sqrt{3}\pi\hbar\gamma\eta}\left[\left(1-\xi+\frac{1}{1-\xi}\right)K_{2/3}(\tilde{\chi}) - \int_{\tilde{\chi}}^\infty dx\, K_{1/3}(x)\right] \tag{12}$$

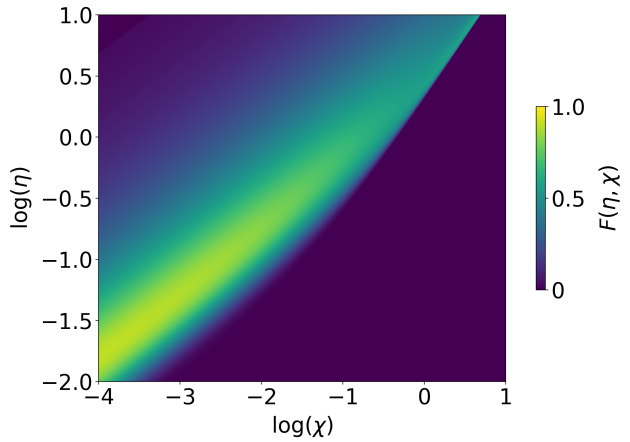

Fig. 3—Synchrotron function [Eq. (9)] versus quantum parameters η and χ.

where $\tilde{\chi} = 2\xi/3\eta(1-\xi)$, $\xi = \chi_\gamma/\eta$, and we have defined $\chi_\gamma = 2\chi$ with χ given by Eq. (11). We note that this distribution is simply an alternate form of Eq. (8). The photon is emitted in the electron's propagation direction,[2] and OSIRIS accounts for the subsequent momentum recoil using the classical radiation force of Landau and Lifshitz [9, 10, 27].

3.2.2 EPOCH

EPOCH is an open source PIC code developed and maintained by researchers at the University of Warwick. It offers a variety of modules for modeling bremsstrahlung radiation, trident pair creation, and nonlinear Compton scattering.

The Monte-Carlo emission algorithm in EPOCH operates as follows. The Vlasov equations for the electron/positron and photon distribution functions $f_\pm(\vec{x},\vec{p},t)$ and $f_\gamma(\vec{x},\vec{k},t)$, respectively, are solved. Then, the cumulative probability of emission function, defined by: $P(t) = 1 - \exp(-\tau_{\rm em})$ where $\tau_{\rm em}$ is the optical depth of the electron in question, is set equal to a pseudo-random number uniformly distributed in $[0,1]$, and inverted to obtained $\tau_{\rm em}$. This is the optical depth at which the electron will emit a photon. The code then numerically solves the optical depth evolution equation,

$$\tau(t) = \int_0^t \lambda[\eta(t')]\,dt' \tag{13}$$

via first-order Eulerian integration, where λ is the emission rate of the process in question (in our case, nonlinear Compton scattering) and $\eta = E_{\rm rf}/E_s$ as in Eq. (2). Once the condition $\tau \geq \tau_{\rm em}$ is met, the electron emits a photon with a quantum parameter obeying the distribution of Eq. (8) (see Ref. [28]).

3.3 Particle Merging

In physical situations where the total number of macro-particles can grow exponentially fast, such as repeated photon emission and pair formation (a QED cascade), merging macro-particles together is critical

[2]To be more precise, the emitted photon direction is constrained within a cone subtending an angle $\Delta\theta \sim \gamma^{-1}$, but since γ is typically very large, it is safe to assume $\Delta\theta \simeq 0$.

to prevent memory overflow. We mention briefly here that a particle merging algorithm has been developed for OSIRIS [29]. In the input deck, the user specifies a maximum number of macro-particles to allow in the simulation in addition to a frequency with which the code will check the number of macro-particles. The main point is that OSIRIS merges particles that are close in coordinate and momentum space, and creates two macro-particles in order to conserve both energy and momentum. The total weight is also conserved.

3.4 Covariant Propagation

The standard Boris pusher implemented in most PIC codes develops serious errors in the presence of an extreme field unless the time-step used is very small. We mention here that a covariant pusher which eliminates this error has been developed [30], but was not implemented in our simulation runs. The use of PIC codes to model laser-plasma interaction in the intensity regime of upcoming multi-petawatt lasers necessitates eventual scrutiny of the pusher algorithm [31, 32].

3.5 Simulation Setup

The basic simulation setup for studying photon emission is shown in Fig. 4. A high-powered laser pulse (wavelength $\lambda = 1\ \mu$m) impinges on an overcritical plasma whose longitudinal density profile is shown. The pre-plasma region, which has a characteristic exponential length $\ell_{\|}$, serves to induce relativistic self-focusing and absorb the pulse energy. It is the primary region in which γ-rays are generated. Experimentally, it can be produced by ablating a solid foil target using, for example, the amplified spontaneous emission pedestal or a powerful ionizing pre-pulse. Self-focusing the pulse is desired in this scenario in order to increase the intensity, and consequently the cross section for nonlinear Compton scattering, and extend the interaction region over which the mechanism occurs.

A phenomenological relationship proposed in Ref. [19] gives the following relationship between the incident pulse power and peak plasma density:

$$P_L \simeq 10^2\ \text{PW} \times n_{\text{cr}}/n_e \tag{14}$$

where n_e is the electron density and $n_{\text{cr}} = m\omega_p^2/4\pi e^2$ is the (non-relativistic) critical density associated with plasma frequency ω_p. Thus, a 10 PW pulse should strike a target of maximum density $10\,n_{\text{cr}}$ to maximize the laser-to-gamma energy conversion efficiency. Note that in the pulse reference frame, the plasma is actually under-dense because of relativistic-induced transparency. The Lorentz factor of electrons ponderomotively accelerated by a plane-polarized wave of amplitude a_0 is $\gamma = \sqrt{1+a_0^2/2}$, and the relativistically-corrected critical density is $n'_{\text{cr}} = \gamma m\omega_p^2/4\pi e^2$.

The pulse duration should be such that the longitudinal extent of the intensity profile is comparable in size to the plasma target. An extremely short pulse will only accelerate electrons in the pre-plasma, leaving no background photons to be absorbed, while a very long pulse will hinder the energy absorption efficiency. Assuming the intensity is sufficiently high, the target will be entirely obliterated in the long-pulse scenario. As we show in the next section, the slab target thickness ℓ_S also plays a key role in the γ-ray generation mechanism. Overall, the process is quite sensitive to a number of different parameters, such as the pulse duration, pre-plasma length, target density, and peak power/intensity.

Two-dimensional simulations were performed both locally and on the National Energy Research Scientific Computing Center (NERSC) Cori computing cluster. Typical simulations used anywhere between 40

and 160 cores, and ran for a couple of days to one week. With the QED module, the need to resolve emission processes imposes an additional time-step constraint:

$$\Delta t < \Delta t_{\rm QED} = 1/{\rm Max}(dN_\gamma/dt)$$

where dN_γ/dt is the photon emission rate. The result of calculations based on the theory of [33] indicates that for $a_0 = 300$, the electron quantum parameter is $\eta \simeq 1.54 \times 10^{-2}$ and the nonlinear Compton emission frequency is approximately 50 THz (once every 20 fs). In our simulations, we typically employed time-steps between 2 and 5 attoseconds. As for the grid resolution, we resolved the high-density target by using

$$0.5/k_p^* < \Delta x, \Delta y < 1/k_p^*$$

in which $k_p^* = \omega_p^*/c$ is the plasma wavenumber of the maximum density, $\omega_p^* = \sqrt{4\pi n_{\rm max} e^2/m}$, and m is the bare electron mass. With such a grid resolution, the Courant condition limits the time-step to approximately 80 attoseconds.

4. RESULTS

Early in our investigation, we performed parametric scans in OSIRIS to understand the dependence of the total γ energy on characteristics of the laser pulse and plasma target. In particular, we varied the pre-plasma length, target slab thickness, incident pulse duration, and laser intensity and polarization. A simulation based on the parameters of Ref. [19] was also performed, in OSIRIS and EPOCH, and forms the basis of our comparison between the two PIC codes. In the subsections to follow, each set of simulations are discussed.

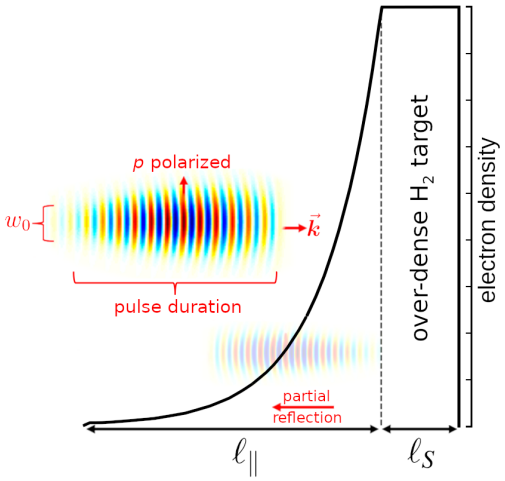

Fig. 4—Illustration of the laser pulse and longitudinal plasma density profile.

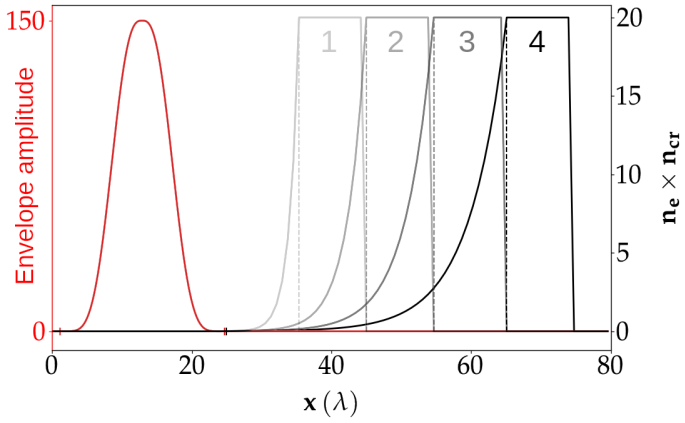

Fig. 5—Laser pulse intensity envelope (red) and plasma profiles (black). Each subcase corresponds to the indicated multiple of 10 μm for ℓ_x.

4.1 Gamma-ray Energy Dependence Parametric Scan

4.1.1 Varying pre-plasma length

In this set of simulations, a 30 fs pulse with an intensity of 3×10^{22} W/cm^2 ($a_0 = 150$) and a waist of 5λ is used. The hydrogen plasma has a peak density of 20 $n_{\rm cr}$, the length of the target slab is $\ell_S = 10$ μm, and the pre-plasma length $\ell_\parallel$ is varied between 10 and 40 μm. The cutoff energy for tracked photons, used here and in all other simulations, was set to $\mathscr{E}_{\rm min} = 51.1$ keV. In Fig. 5, the laser intensity and target profiles are shown for each of the subcases. In Fig. 6, the variation in total γ energy versus time is provided. Note that $\mathscr{E}_\gamma$ has units of kJ/cm as this is a two-dimensional configuration. The gradual decay in energy for $t \gtrsim 200$ fs is due to photons leaving the simulation domain (reflecting and absorbing boundary conditions were used for the transverse and longitudinal boundaries, respectively). The dependence of the peak γ energy on pre-plasma length increases considerably between $\ell_\parallel = 10\lambda$ and $\ell_\parallel = 20\lambda$, but then plateaus for longer pre-plasma lengths (see Table 1). This suggests that a long pre-plasma is needed to absorb the pulse. In Fig. 7, a snapshot ($t \simeq 290$ fs) of the electron charge density is shown. The laser pulse bores completely through the plasma, though its energy is mostly depleted (less than 10% of the total field energy remains after interaction).

Table 1—Energy conversion efficiency vs. pre-plasma length

Subcase	Efficiency
$\ell_\parallel = 10\lambda$	17.85 %
20λ	19.77 %
30λ	20.61 %
40λ	20.80 %

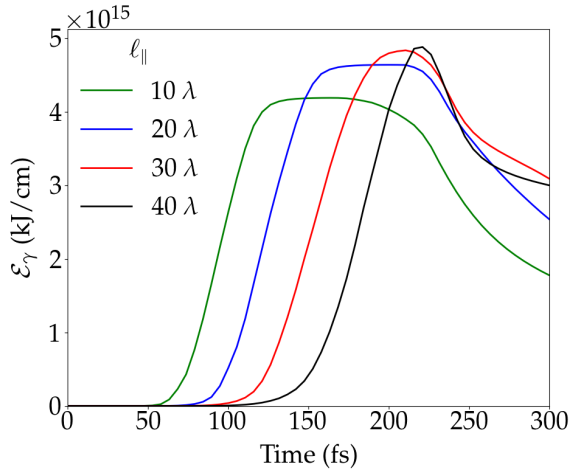

Fig. 6—Variation in total γ energy versus time.

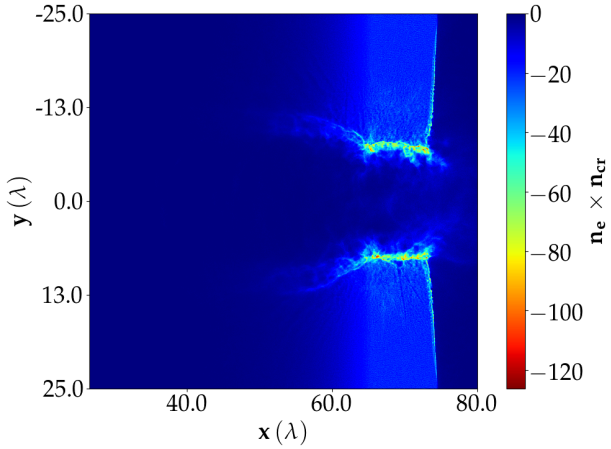

Fig. 7—Electron charge density after laser-plasma interaction; $\ell_\parallel = 40\lambda$ case.

4.1.2 Varying target thickness

In this parametric scan, the same laser properties considered in Section 4.1.1 were used. The target had a peak density of 20 $n_{\rm cr}$ and a 30λ pre-plasma length. The slab thickness ℓ_S was varied between 10 and 30 μm. The laser-to-gamma energy conversion efficiency increased by approximately 2% when ℓ_S was increased from 10 μm to 20 μm, but an additional 10 μm increase of the target slab had little effect. This indicates that a sufficiently thick target is required to absorb the pulse, and provide electrons capable of emitting γ-rays. In Table 2, the energy conversion for each subcase is provided.

Table 2—Energy conversion efficiency vs. target thickness

Subcase	**Efficiency**
$\ell_S = 10\lambda$	20.38 %
20λ	22.20 %
30λ	22.25 %

4.1.3 Varying laser pulse duration

For this set of simulations, all laser pulse properties considered in Section 4.1.1 were used except for the FWHM pulse duration, which was varied from 40 fs to 60 fs. The pulse amplitude was held fixed at $a_0 = 150$. The plasma profile used was equivalent to Subcase 3 of Section 4.1.1 ($\ell_{\parallel} = 30\lambda$, 20 $n_{\rm cr}$ peak density, and so on). Here, the conversion efficiency decayed monotonically for increasing values of the laser pulse duration. This result is in agreement with Eq. (14), and the conclusion that reducing the power hinders the efficiency of the process. With a longer pulse duration, electrons and ions also do not gain as much energy, and it has been observed that for $\tau_{\rm FWHM} = 60$ fs the pulse retains 40% of its initial energy after interaction.

Table 3—Energy conversion efficiency vs. pulse duration

Subcase	**Efficiency**
$\tau_{\rm FWHM} = 40$ fs	19.57 %
50 fs	18.21 %
60 fs	16.36 %

4.1.4 *Varying laser intensity*

In this case, the laser intensity values provided in Table 4 were considered. The pulse duration was 30 fs, and the plasma profile used was that of Subcase 3 from Section 4.1.1 There is an approximately 2% increase in conversion efficiency for every 5 PW of laser power, see Table 5.

Table 4—Laser intensity parameters

Amplitude, a_0	**Intensity**	**Power***
175	4.19×10^{22} W/cm^2	16.5 PW
200	5.47×10^{22} W/cm^2	21.5 PW
225	6.93×10^{22} W/cm^2	27.2 PW

*Calculated assuming axial symmetry; waist $w_0 = 5\lambda$.

Table 5—Energy conversion efficiency vs. laser intensity

Subcase	**Efficiency**
$a_0 = 175$	23.84 %
200	25.92 %
225	27.53 %

4.1.5 *Varying laser polarization*

Here, we employed all laser pulse and plasma profile properties from Section 4.1.1, except the polarization was varied in the following manner. Let us take Subcase 1 in this section to be Subcase 3 from Section 4.1.1, in which the laser is polarized in the E_y (transverse) direction. Subcase 2 considered a 45° polarization in the y-z plane (transverse and orthogonal axes), while Subcase 3 used a laser polarized completely in the E_z direction. Lastly, Subcase 4 employed a circularly-polarized beam. The energy conversion efficiency is listed in Table 6 below. The efficiency decreases as the laser polarization leaves the plane spanned by the transverse and longitudinal axes, but increases significantly for a circularly-polarized beam. Thus, in next-generation multi-petawatt laser facilities, it may be more efficient to employ a circularly-polarized beam to study this process.

Table 6—Energy conversion efficiency vs. laser polarization

Subcase	**Efficiency**
1, linear y	20.61 %
2, linear y-z	18.17 %
3, linear z	14.27 %
4, circular	26.39 %

4.2 High-efficiency Case: OSIRIS vs. EPOCH

It has been reported that under certain conditions 30% of the incident pulse energy can be converted into γ-rays [19]. We simulated this case in OSIRIS and EPOCH, and obtained broad agreement between the two codes and published results. Multiple aspects of the γ-flash phenomenon will be discussed using this simulation case. The setup under consideration is shown in Fig. 8. A 30 fs, 20 PW pulse ($I \simeq 2\times10^{23}$ W/cm^2, $w_0 = 5\lambda$) polarized in the transverse direction is incident on a 20 $n_{\rm cr}$ target with an exponentially decaying pre-plasma of characteristic length $\ell_{\parallel} = 40\lambda$, and slab thickness $\ell_S = 10\lambda$. The fractional energy contained in the field, charged particles, and photons versus time is shown in Figs. 9 and 10 for OSIRIS and EPOCH, respectively. The peak conversion efficiencies are 33% (OSIRIS) and 30% (EPOCH). We attribute the slight difference to subtleties in the algorithm, and the fact that the emission process is stochastic.

The energy spectrum for each type of particle, which is approximately the same for both codes, is provided in Fig. 11. From this, we see see that we obtain at most $\mathscr{E}_\gamma \simeq 750$ MeV photons. In Fig. 12, the variation of the maximum normalized field amplitude a_0 with time is shown. The pulse amplitude reaches $a_0 \simeq 560$ at the front of the high-density slab, while the radiation reaction friction force parameter $a_0\varepsilon_{\rm rad}^{1/3}$ (right-hand axis) increases from 0.75 through 1.25, which is within the optimal range of values to maximize the nonlinear Compton scattering cross section (see Section 2.1). Theoretical considerations indicate that the power radiated by γ-rays occurs on a timescale proportional to the pulse duration [34], which is consistent with our observations (Fig. 13). In Fig. 14, the spectrum of radiated photons is shown at $t = 100$ fs and 400 fs. From this data, it is apparent that high-energy photons dominate early in the simulation, but then the tail of low-energy photons steadily rises. In Fig. 15, the momentum phase-space distribution of electrons is provided, and in Fig. 16 the electron quantum parameter is plotted during the period of maximum electron energy gain. The most energetic electrons are scattered in the forward direction, and the instant of peak photon radiation coincides with the observed increase in the total electron quantum parameter. The average γ energy and number density in the pre-plasma and target are shown in Fig. 17 at the instant of peak photon emission. Lastly, Fig. 18 shows the angular distribution of emitted γ-rays with the energy cutoff conditions $\mathscr{E}_\gamma/mc^2 > 0$ and $\mathscr{E}_\gamma/mc^2 > 100$. At low energy, photons are emitted isotropically, while the highest-energy γ-rays are emitted in the direction of pulse propagation. This is consistent with the fact that the highest energy electrons are ponderomotively accelerated in the forward direction.

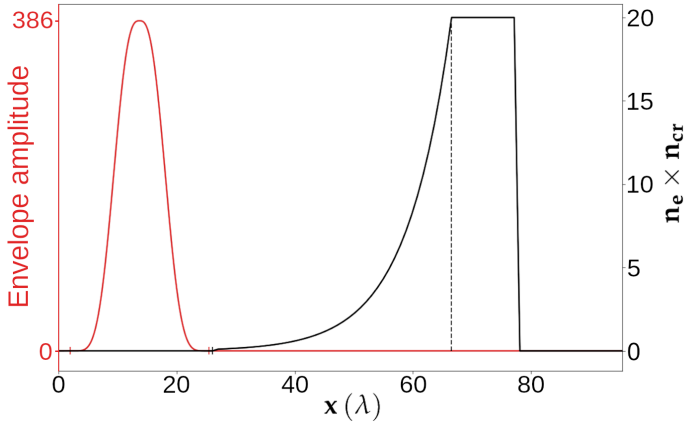

Fig. 8—Simulation setup for the high-efficiency case.

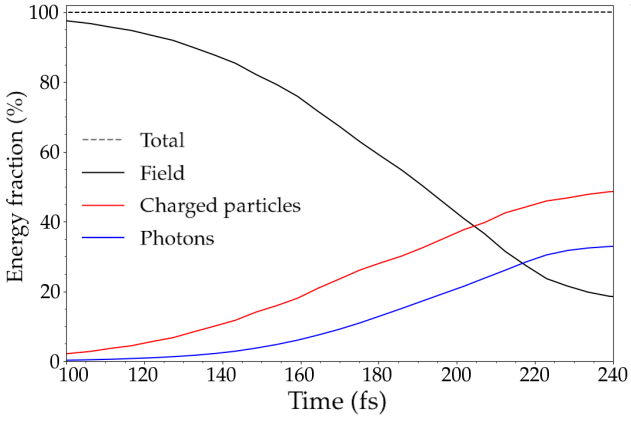

Fig. 9—OSIRIS: Energy fraction vs. time.

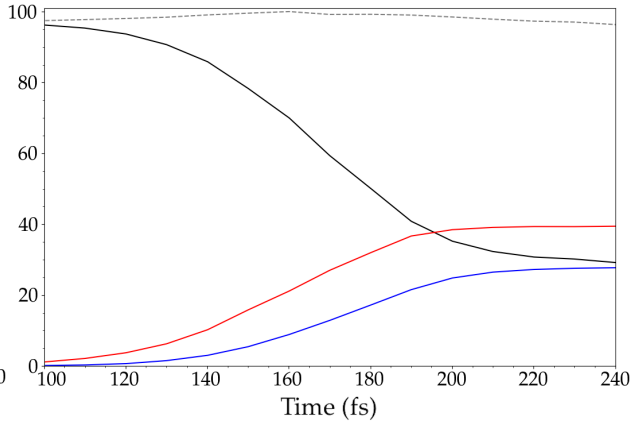

Fig. 10—EPOCH: Energy fraction vs. time.

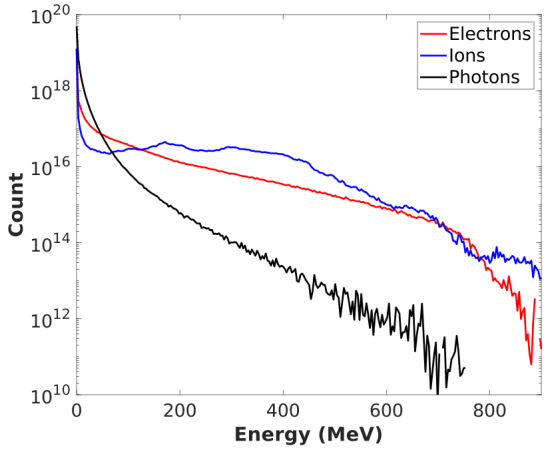

Fig. 11—Particle energy spectrum.

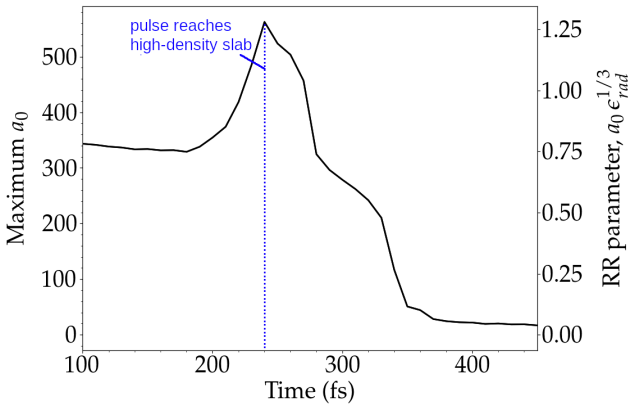

Fig. 12—Peak field amplitude and radiation-reaction parameter vs. time.

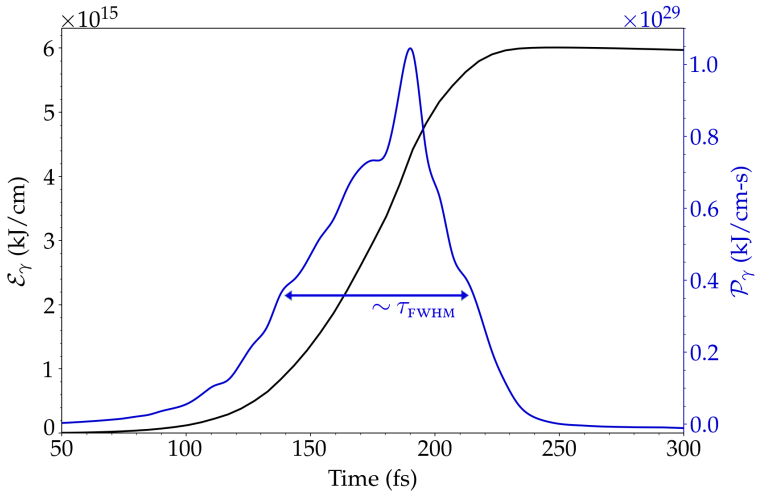

Fig. 13—Time dependence of photon energy $\mathscr{E}_\gamma$ (black) and radiated power P_γ (blue).

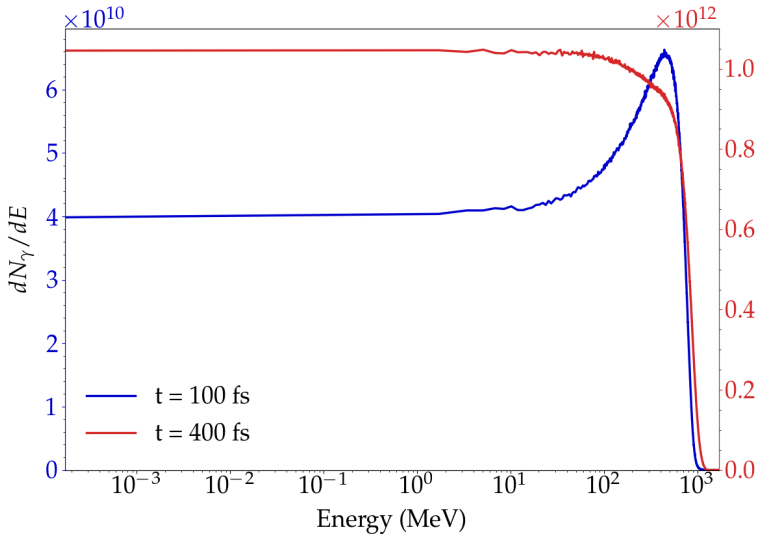

Fig. 14—Spectrum of radiated emission by electrons.

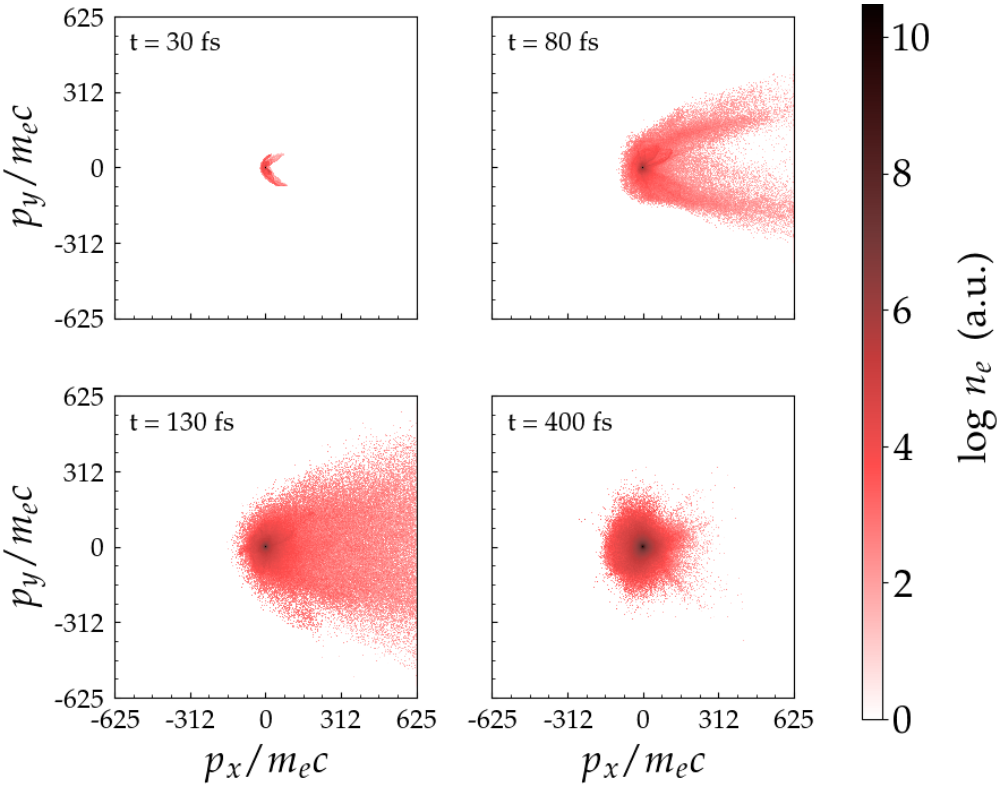

Fig. 15—Electron momentum distribution at the indicated times.

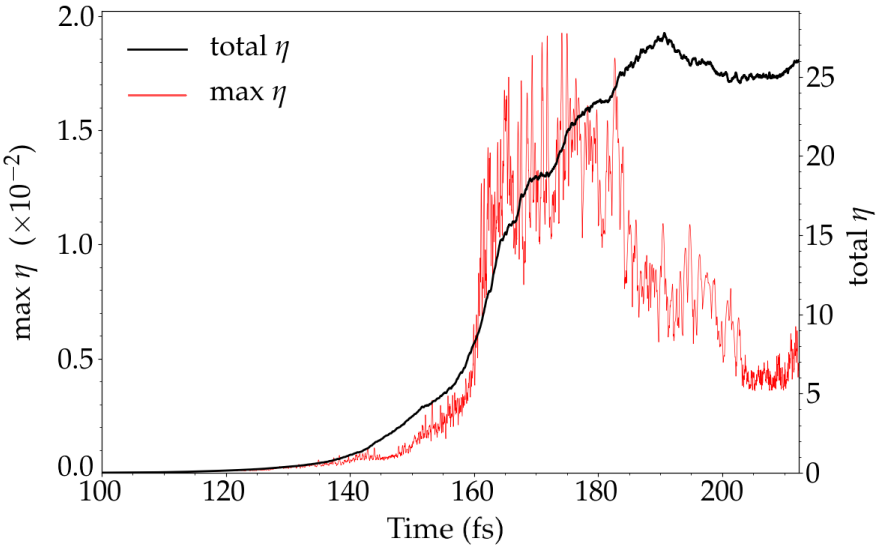

Fig. 16—Variation of the total (black) and maximum (red) electron quantum parameter.

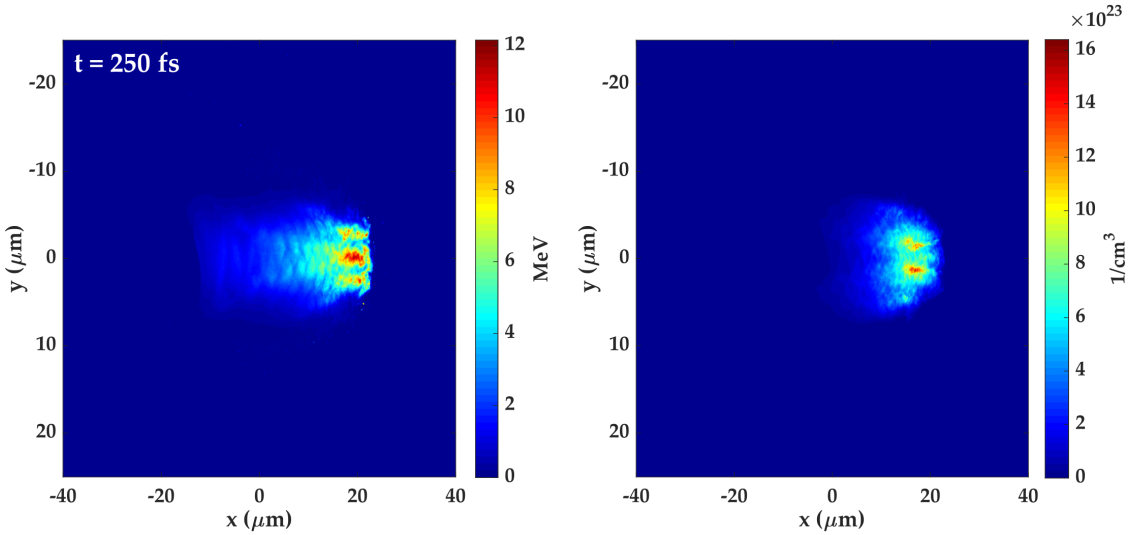

Fig. 17—Average γ energy (left) and density (right) at the instant of peak photon radiation.

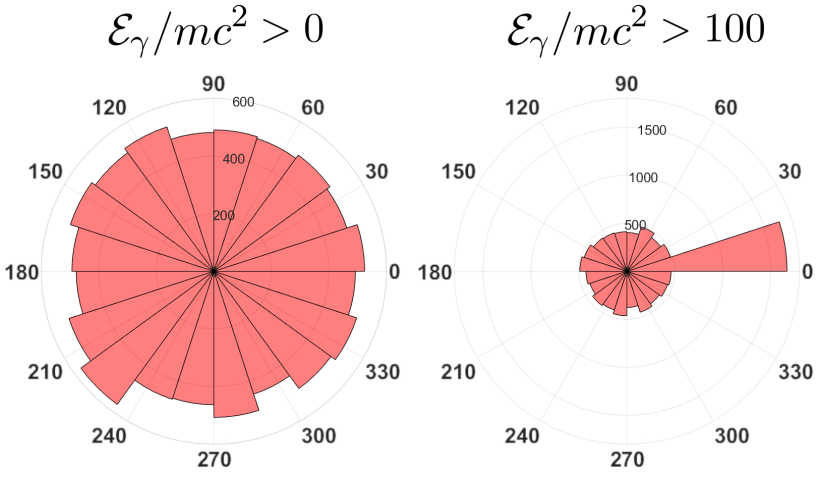

Fig. 18—Angular distribution of emitted γ-rays with the indicated energy cutoff conditions.

5. CONCLUSION

The interaction of a high-intensity pulse with an overcritical plasma target results in γ-ray emission by the nonlinear Compton scattering process. We demonstrated that under the right conditions, this process can be made extremely efficient, allowing for the conversion of roughly one-quarter of the incident pulse energy into high-energy photons. Moreover, we showed that two state-of-the-art PIC codes are in agreement when it comes to the magnitude of the energy conversion efficiency.

Our simulations highlight multiple aspects of this nonlinear process which warrant further investigation. The forward-propagating electrons are responsible for the γ-rays of highest energy, yet the quantum parameter is maximized for an electron that is counter-propagating with the Poynting vector (see Appendix A). Therefore, we suspect that the efficiency of γ-ray emission relies heavily on the intensity of reflected radiation. A series of parametric scans intended to optimize the reflected pulse intensity, which will primarily depend on the target geometry and plasma density, can elucidate the dependence between the back-propagating field strength and γ-ray conversion efficiency, and help to derive phenomenological scaling laws.

It is also interesting to consider whether a QED-plasma can be produced by counter-propagating a second pulse to interact with the ultra-relativistic electrons and γ-rays produced by the first pulse. The pair-production efficiency then factors into the plasma dynamics, in addition to quantities such as the counter-propagating pulse intensity, duration, and delay. In the near future, this double-pulse configuration may be explored.

ACKNOWLEDGMENTS

This work was supported by the US DOE Office of Science under Interagency Agreement number 89243018SSC000006, and the Directed Energy Society's Directed Energy Summer Internship program. This research was conducted while A. W. D. held an NRC Research Associateship award at the Naval Research Laboratory.

REFERENCES

1. J. Bromage et al., "Technology development for ultra-intense all-OPCPA systems," *High Power Laser Science and Engineering* **7**, E4 (2019).
2. A. Di Piazza, C. Müller, K. Z. Hatsagortsyan, and C. H. Keitel, "Extremely high-intensity laser interactions with fundamental quantum systems," *Rev. Mod. Phys.* **84**, 1177 (2012).
3. B. M. Hegelich, G. Mourou, and J. Rafelski, "Probing the quantum vacuum with ultra intense laser pulses," *Eur. Phys. J. Spec. Top.* **223**, 1093–1104 (2014).
4. P. Zhang, S. S. Bulanov, D. Seipt, A. V. Arefiev, and A. G. R. Thomas, "Relativistic plasma physics in supercritical fields," *Phys. Plasmas* **27**, 050601 (2020).
5. M. J. Bernstein and G. G. Comisar, "X-ray production in laser-heated plasmas," *J. Appl. Phys.* **41**, 729 (1970).
6. D. J. Stark, T. Toncian, and A. V. Arefiev, "Enhanced multi-MeV photon emission by a laser-driven electron beam in a self-generated magnetic field," *Phys. Rev. Lett.* **116**, 185003 (2016).
7. T. Wang et al., "Power scaling for collimated γ-ray beams generated by structured laser-irradiated targets and its application to two-photon pair production," *Phys. Rev. Applied* **13**, 054024 (2020).
8. V. I. Ritus, "Quantum effects of the interaction of elementary particles with an intense electromagnetic field," *Journal of Soviet Laser Research* **6**, 497–617 (1985).
9. L. D. Landau and E. M. Lifshitz, *The Classical Theory of Fields* (Pergamon Press, London, 1988).
10. V. B. Berestetskii, E. M. Lifshitz, and L. P. Pitaevskii, *Quantum Electrodynamics* (Pergamon Press, London, 1980).
11. B. Hafizi, D. F. Gordon, and D. Kaganovich, "Pair creation with strong laser fields, Compton scale X rays, and heavy nuclei," *Phys. Rev. Lett.* **122**, 233201 (2019).
12. S. Deng et al., "Modeling of ionization physics with the PIC code OSIRIS," *AIP Conference Proceedings* **647**, 219 (2002).
13. T. D. Arber et al., "Contemporary particle-in-cell approach to laser-plasma modelling," *Plasma Physics and Controlled Fusion* **57**, 11 (2015).
14. F. Mackenroth and A. Di Piazza, "Nonlinear Compton scattering in ultrashort laser pulses," *Phys. Rev. A* **83**, 032106 (2011).
15. S. V. Bulanov et al., "On the problems of relativistic laboratory astrophysics and fundamental physics with super powerful lasers," *Plasma Phys. Rep.* **41**, 1 (2015).

16. W. H. Furry, "On bound states and scattering in positron theory," *Physical Review* **81**, 1 (1951).

17. D. M. Volkov, "Über eine Klasse von Lösungen der Diracschen Gleichung," *Z. Phys.* **94**, 250 (1935).

18. A. Henderson et al., "Ultra-intense gamma-rays created using the Texas Petawatt Laser," *High Energy Density Physics* **12**, 46–56 (2014).

19. K. V. Lezhnin, P. V. Sasorov, G. Korn, and S. V. Bulanov, "High power gamma flare generation in multi-petawatt laser interaction with tailored targets," *Phys. Plasmas* **25**, 123105 (2018).

20. C. Bamber et al., "Studies of nonlinear QED in collisions of 46.6 GeV electrons with intense laser pulses," *Phys. Rev. D* **60**, 092004 (1999).

21. T. G. Blackburn and M. Marklund, "Nonlinear Breit-Wheeler pair creation with bremsstrahlung γ rays," *Plasma Phys. Control. Fusion* **60**, 054009 (2018).

22. J. D. Bjorken and S. D. Drell, *Relativistic Quantum Mechanics* (McGraw-Hill, 1964).

23. C. K. Birdsall and C. K. Langdon, *Plasma Physics via Computer Simulation* (IOP Publishing, London, 2004).

24. R. W. Hockney and J. W. Eastwood, *Computer Simulation Using Particles* (IOP Publishing, London, 1989).

25. C. P. Ridgers et al., "Dense electron-positron plasmas and ultraintense γ rays from laser-irradiated solids," *Phys. Rev. Lett.* **108**, 165006 (2012).

26. J. G. Kirk, A. R. Bell, and I. Arka, "Pair production in counter-propagating laser beams," *Plasma Phys. Control. Fusion* **51**, 085008 (2009).

27. M. Vranic et al., "Quantum radiation reaction in head-on laser-electron beam interaction," *New J. Phys.* **18**, 073035 (2016).

28. C. P. Ridgers et al., "Modelling gamma ray emission and pair production in high-intensity laser-matter interactions," *J. Comp. Phys.* **260**, 273 (2014).

29. M. Vranic, T. Grismayer, J. L. Martins, R. A. Fonseca, and L. O. Silva, "Particle merging algorithm for PIC codes," *Comp. Phys. Comm.* **191**, 65–73 (2015).

30. D. F. Gordon, B. Hafizi, and J. Palastro, "Pushing particles in extreme fields," *AIP Conference Proceedings* **1812**, 050002 (2017).

31. J. L. Vay, "Simulation of beams or plasmas crossing at relativistic velocity," *Phys. Plasmas* **15**, 056701 (2008).

32. A. Higuera and J. Cary, "Structure-preserving second-order integration of relativistic charged particle trajectories in electromagnetic fields," *Phys. Plasmas* **24**, 052104 (2017).

33. N. V. Elkina et al., "QED cascades induced by circularly polarized laser fields," *Phys. Rev. ST Accel. Beams* **14**, 054401 (2011).

34. T. Nakamura et al., "High-power γ-ray flash generation in ultraintense laser-plasma interactions," *Phys. Rev. Lett.* **108**, 195001 (2012).

Appendix A

ON THE ELECTRON QUANTUM PARAMETER

Recall the definition of η, which characterizes the strength of nonlinear QED effects for electrons,[A.1]

$$\eta = \frac{e\hbar}{m^3c^4}|F_{\mu\nu}p^\nu| \tag{2}$$

where $p^\nu = (\mathscr{E}/c, \vec{p})$ is the 4-momentum of an electron of energy $\mathscr{E} = \gamma mc^2$ and momentum $\vec{p} = \gamma m\vec{v}$, and $F_{\mu\nu}$ is the electromagnetic field tensor. We wish to evaluate η for typical field magnitudes in the case of (1) an electron beam counter-propagating with a plane electromagnetic wave, and (2) an electron beam in a static magnetic field.

A.1 Plane Electromagnetic Wave

Consider an electron beam which is oriented in the $-\hat{z}$ direction, with the electromagnetic wave propagating at a relative angle θ (Fig. A1). Then

$$|F_{\mu\nu}p^\nu| = \sqrt{\big(mcE\sin\theta\big)^2 + \big((\varepsilon/c)E\cos\theta + pB\big)^2} \tag{A1}$$

and

$$\eta_{\,\mathrm{EM}}(\theta) = \sqrt{(E/E_s)^2\sin^2\theta + \big(\gamma(E/E_s)\cos\theta + \gamma\beta B/E_s\big)^2} \tag{A2}$$

where $\beta = v/c$, and the electric and magnetic field magnitudes are denoted E and B, with E_s the Schwinger critical field. Note that an e-beam which is anti-parallel to the incident pulse has the highest efficiency, in the sense that it maximizes $\eta_{\,\mathrm{EM}}$. In this case, taking $\theta = 0$ in Eqs. (A1) and (A2) gives:

$$|F_{\mu\nu}p^\nu| = (\varepsilon/c)E + pB \tag{A3}$$

and

$$\eta_{\,\mathrm{EM}} = \frac{\gamma E}{E_s} + \frac{\gamma\beta B}{E_s} \tag{A4}$$

In Section 4, we showed that the normalized field amplitude can reach as high as $a_0 \simeq 300$ as a result of relativistic self-focusing in the plasma, which corresponds to $E = 9.63\times10^{14}$ V/m at $\lambda = 1$ μm. A highly energetic e-beam ($\beta = 0.99$) encountering a field of such intensity has a quantum parameter

$$\eta_{\,\mathrm{EM}} \simeq 10^{-2}$$

see Fig. A2

[A.1] photon emission being of particular interest.

A.2 Static Magnetic Field

For an e-beam in a static magnetic field, the quantum parameter $\eta_{\rm B}$ will be non-zero only when $\vec{B}$ is transverse to the beam's propagation direction. In such a case,

$$|F_{\mu\nu}p^{\nu}| = pB \tag{A5}$$

and

$$\eta_{\rm B} = \frac{\gamma\beta B}{E_s} \tag{A6}$$

If the magnetic field is 0.2 MT, as simulations involving magneto-bremsstrahlung radiation indicate [A7], then an e-beam of the same energy considered above has a quantum parameter of

$$\eta_{\rm B} \simeq 3.2 \times 10^{-4}$$

Note that $\eta_{\rm B}$ is 2 orders of magnitude smaller than the quantum parameter due to an e-beam and an electromagnetic wave, $\eta_{\rm EM}$.

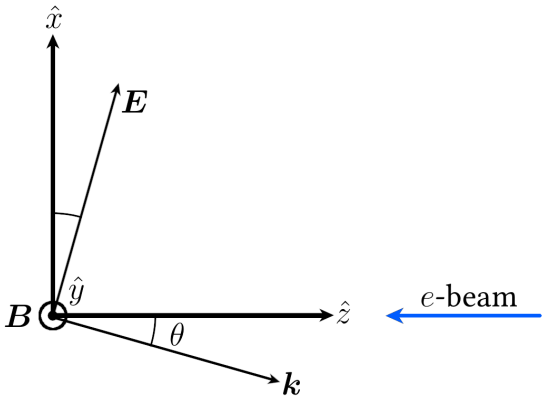

Fig. A1—Geometrical diagram used for the calculation of the quantum parameter η vs. angle θ.

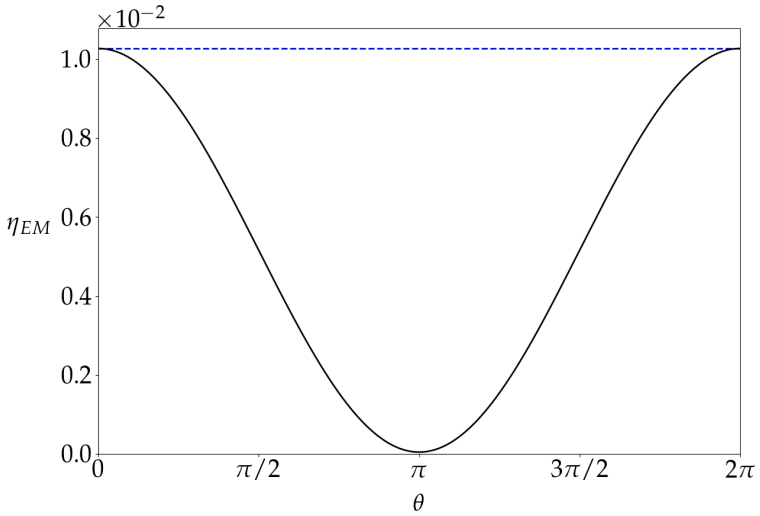

Fig. A2—Quantum parameter as a function of angle between the e-beam and incident wave. Dashed blue: Maximum efficiency case, $\theta = 0$.